第 29 卷　第 5 期
2021 年 5 月

光学 精密工程
Optics and Precision Engineering

Vol. 29　No. 5
May 2021

文章编号　1004-924X(2021)05-1024-19

传感器倾斜对于偏振光航向解算的影响

梁华驹[1]，白宏阳[1*]，周　同[2]，沈　凯[3]
（1. 南京理工大学 能源与动力工程学院，江苏 南京 210094；
2. 南京理工大学 机械工程学院，江苏 南京 210094；
3. 北京理工大学 自动化学院，北京 100081）

摘要：昆虫利用偏振光获取航向，经典的偏振光航向角解算方法都需要偏振光传感器指向天顶点。针对这一问题，设计了基于太阳位置模型、瑞利天空模型和虚拟偏振传感器的偏振光航向解算仿真系统，详细研究了4种典型的基于偏振光的航向解算方法在仅俯仰倾斜、仅滚转倾斜、俯仰和滚转倾斜条件下的误差特性。最后，仿真和实验均表明，4种典型方法在受到倾斜干扰时，其航向解算误差具有一致性的规律性，而且解算误差不仅受倾角的影响，还受太阳高度角，太阳与偏振传感器相对位置的影响。本文的结果不仅可以用于量化估计传感器倾斜所引起的航向角解算误差，还可用于补偿修正传感器倾斜导致的航向角解算误差。

关　键　词：偏振光学；航向解算；传感器倾斜；大气偏振模式

中图分类号：TN29　　**文献标识码：**A　　**doi：**10.37188/OPE.20212905.1024

Impact of sensor tilt on bio-inspired polarized skylight orientation determination

LIANG Hua-ju[1], BAI Hong-yang[1*], ZHOU Tong[2], SHEN Kai[3]

(1. *School of Energy and Power Engineering, Nanjing University of Technology,*
Nanjing 210094, *China*;
2. *School of Mechanical Engineering, Nanjing University of Technology, Nanjing* 210094, *China*;
3. *School of Automation, Beijing University of Technology, Beijing* 100081, *China*)
* *Corresponding author, E-mail: hongyang@njust.edu.cn*

Abstract: Inspired by many insects, several polarized skylight orientation determination approaches have been proposed. However, almost all of these approaches always require polarization sensors pointing to the zenith of the sky dome. Therefore, the influence of sensor tilts (not pointing to the sky zenith) on bio-inspired polarization orientation determination needs to be analyzed urgently. Aiming at solving this problem, a polarization compass simulation system is designed based on a solar position model, the Rayleigh sky model, and a hypothetical polarization imager. Then, the error characteristics of four typical orientation determination approaches are investigated in detail under the pitch tilt condition, roll tilt condition, and both pitch and roll tilt conditions. Finally, simulations and field experiments indicate that the orientation errors of the four typical approaches are highly consistent when they are subjected to tilt interference;

收稿日期：2020-07-31；**修订日期：**2020-09-01.
基金项目：国家自然科学基金资助项目(No. U2031138)

the errors are affected by not only the degree of inclination but also the solar altitude angle and the relative position between the Sun and polarization sensor. The results of this study can be used to estimate the orientation determination error caused by sensor tilts and correct this type of error.

Key words: polarization optics; orientation determination; sensor tilts; skylight polarization pattern

1 Introduction

Traditional navigation systems such as the inertial navigation system, global position system (GPS), and geomagnetic navigation system (GNS) play a key role in the navigation of aircraft, robots, missiles, and vehicles. Inertial navigation systems have many advantages, whereas gyroscopes and accelerometers are usually prone to drift and noise, which may cause error accumulation over time[1]. In addition, although the GPS is a real-time and cost-effective locating system, GPS signals can be easily jammed owing to the presence of disturbances[2-3]. GNSs are sensitive to electromagnetic interference[4]. With the rapid advancement of human society, there is a need to design a highly precise, autonomous, reliable, and robust navigation system.

The navigation behavior of animals provides us with new ideas regarding navigation[5-6]. Desert ants rely on the predictable pattern of polarized light in the sky to find their way back home in hostile environments[7-8]. Honey bees detect the polarization of skylights to move from their hives[9-10]. Birds use skylight polarization patterns to calibrate magnetic compasses during their long-range migrations[11]. The dorsal rim area of the compound eyes of locusts is sensitive to polarized skylight, enabling it to estimate its orientation [12-13].

These animals can use polarized light as a compass because of the polarization pattern in the sky[14-15]. Unpolarized sunlight through the Earth's atmosphere produces a skylight polarization pattern[16-19]. Sunlight remains unpolarized until it interacts with atmospheric constituents, and scattering sunlight causes a partial linear pattern of polarization in the sky, which can be well described by the Rayleigh sky model [20-22].

Inspired by the polarization navigation behaviors of animals, several orientation-determination methods have been proposed based on the Rayleigh sky model. Polarization-orientation-determination methods mainly include the following four typical approaches: the zenith, solar meridian and antisolar meridian (SM-ASM), symmetry, and least-squares approaches. The zenith approach is based on calculating the heading angle by measuring the angle of polarization (AOP) at the sky zenith[3,16,23-25]. Because the polarization E-vector along the SM-ASM is consistently perpendicular to the SM-ASM, the heading angle can be calculated by extracting SM-ASM. This approach is called the SM-ASM approach[26-29]. Furthermore, because of the symmetry of the skylight polarization pattern, symmetry detection can be used to determine the orientation. This approach is termed the symmetry approach[30-32]. Finally, the polarization E-vector of the Rayleigh sky model is consistently perpendicular to the solar vector. Therefore, the orientation can be determined by the total-least-square method, which is called the least-square approach[33-36]. However, most of these heading-determination approaches require the polarization sensor to point toward the zenith of the sky dome [37]: the Zenith approach must directly capture the polarization information at the sky zenith; SM-ASM and symmetry approaches require that the reference direction of the AOP be converted to the local meridian using the sky zenith as a reference point; and the least-squares approach requires a known sky zenith dependent coordinate system to determine the orientation accurately.

In actual navigation, the carriers moving in three-dimensional space, such as aerial vehicles, aircraft, and rockets, tilt. Even carriers moving on the ground, such as vehicles and multilegged robots, tilt when the ground is uneven[38-39]. Therefore, the impact of the polarization sensor tilt on bioinspired polarized skylight heading determination requires investigation and detailed discussion[15].

The objective of this paper is to study the impact of the sensor tilt on polarization orientation determination. First, a polarization compass simulation system is designed. Next, based on this simulation system, numerical simulation experiments are performed to investigate the impact of the sensor tilt on the aforementioned four classical heading-determination approaches. Finally, the results of the field experiments are compared with the results of the digital simulation to validate our conclusions.

2 Polarization simulation system

A polarization compass simulation system, depicted in Fig. 1, was designed to study the impact of the sensor tilt on orientation determination.

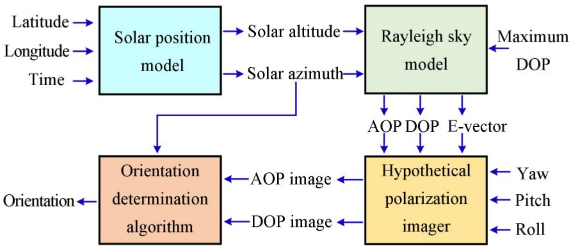

Fig. 1 Polarization compass simulation system. AOP is the angle of polarization, DOP is the degree of polarization, and E-vector is the polarization electric field vector

In addition, the sun azimuth coordinate frame was constructed to describe this system. As depicted in Fig. 2, $ox_g y_g z_g$ is the East-North-Up (ENU) geographic coordinate frame. The y_a axis of the sun azimuth coordinate frame $ox_a y_a z_a$ is aligned with the solar azimuth, z_a axis points to the zenith, and x_a axis completes the right-handed coordinate frame. The sun azimuth coordinate frame rotates around the z_a axis when the solar azimuth changes, and the direction of the y_a axis is always aligned with the direction of the solar azimuth.

The rotation matrix from the ENU coordinate to the sun azimuth coordinate is given by

$$C_g^a = \begin{bmatrix} \cos\varphi_{gS} & -\sin\varphi_{gS} & 0 \\ \sin\varphi_{gS} & \cos\varphi_{gS} & 0 \\ 0 & 0 & 1 \end{bmatrix}, \tag{1}$$

where φ_{gS} is the solar azimuth angle in the ENU coordinate.

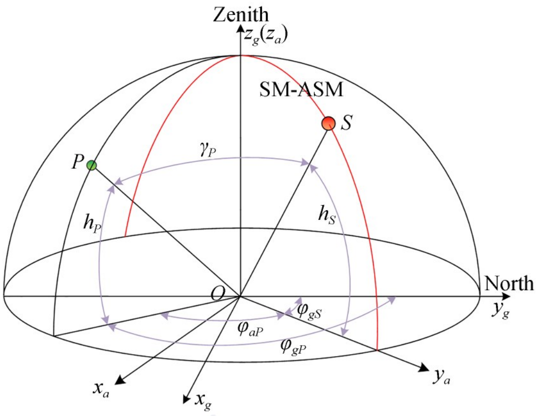

Fig. 2 Coordinate frame: $ox_g y_g z_g$ is the East-North-Up (ENU) geography coordinate frame. $ox_a y_a z_a$ is the sun azimuth coordinate frame. Red circle S represents the sun. Green circle P represents the observation point. The red line SM-ASM represents the solar meridian and anti-solar meridian. h_S is the solar altitude angle. h_P is the altitude angle of P. γ_P is the angle between P and the sun. φ_{gS} is the solar azimuth angle, and φ_{gP} is the azimuth angle of P in the ENU coordinate. φ_{aP} is the azimuth angle of P in the sun azimuth coordinate

2.1 Solar position model

In this section, the solar position is calculated by the relevant astronomical formulae[40-43] to compare the simulation results and field experiments.

Based on relevant astronomical formulae, the position of the sun can be calculated using three angles: solar declination angle δ_S, solar hour angle T_S, and latitude L_O of the observation site. Solving the spherical triangle *S-O-NP* in Fig. 3, the solar altitude angle $h_S \in [0°, 90°]$ and solar azimuth angle $\varphi_{gS} \in [0°, 360°]$ in the ENU coordinate frame are given by

$$\begin{cases} \sin h_S = \sin\delta_S \sin L_O + \cos\delta_S \cos L_O \cos T_S \\ \cos\varphi_{gS} = \dfrac{\sin\delta_S - \mathrm{sinh}_S \sin L_O}{\cos h_S \cos L_O} \end{cases} . \tag{2}$$

By solving the inverse trigonometric function in Eq. (2) and making quadrant judgments, we have:

$$h_S = \arcsin(\sin\delta_S \sin L_O + \cos\delta_S \cos L_O \cos T_S), \tag{3}$$

$$\varphi_{gS} = \begin{cases} \arccos\left(\dfrac{\sin\delta_S - \sin h_S \sin L_O}{\cos h_S \cos L_O}\right) & T_S < 0 \\ 360^\circ - \arccos\left(\dfrac{\sin\delta_S - \sin h_S \sin L_O}{\cos h_S \cos L_O}\right) & T_S > 0 \end{cases} , \tag{4}$$

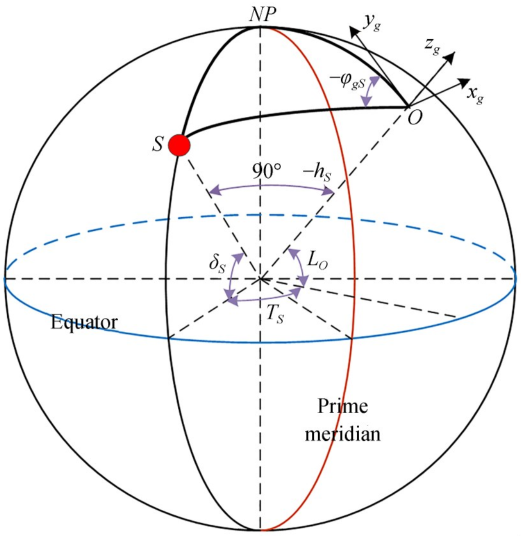

Fig. 3　Celestial sphere, where red circle S is the sun, O is the observation site, NP is the North Pole. δ_S is the solar declination angle, T_S is the solar hour angle, L_O is the latitude of the observation site, h_S is the solar altitude angle and φ_{gS} is the solar azimuth angle in the ENU coordinate

where the formula for the solar declination angle δ_S for 1985 is given by

$$\delta_S = 0.3723 + 23.2567\sin\sigma_S + 0.1149\sin 2\sigma_S - 0.1712\sin 3\sigma_S - 0.758\cos\sigma_S + 0.3656\cos 2\sigma_S + 0.0201\cos 3\sigma_S , \tag{5}$$

where the day angle $\sigma_S = 2\pi(D - D_0)/365.2422$, D is the day of the year, and the spring-equinox time D_0 expressed in days from the particular year (1985) is

$$D_0 = 79.6764 + 0.2422 \times \big(Y - 1985\big) - \mathrm{INT}\big[\big(Y - 1985\big)/4\big], \tag{6}$$

where Y is the year and INT represents the rounding down.

The calculation process for the solar hour angle T_S is given below, where the local standard time S_d of the observation site can be calculated as

$$S_d = S_O + [F_O - 4(120^\circ - Lon_O)]/60. \tag{7}$$

In Eq. (7), for observation site O, S_O and F_O are the hour and minute of the Beijing time, respectively, and Lon_O is the longitude of observation site O.

Then, time error E_t is given as:

$$E_t = 0.0028 - 1.9857\sin\sigma_S + 9.9059\sin 2\sigma_S - 7.0924\cos\sigma_S - 0.6882\cos 2\sigma_S . \tag{8}$$

Next, S_d is corrected by E_t to obtain solar time S_t:

$$S_t = S_d + E_t/60. \tag{9}$$

Finally, the solar hour angle T_S is given as:

$$T_S = \big(S_t - 12\big) \times 15^\circ. \tag{10}$$

In short, using the above formulae, the solar azimuth angle and solar altitude angle can be calculated.

2.2　Rayleigh sky model

The Rayleigh sky model predicts the degree of polarization (DOP) of the sky polarization properties[3] as:

$$DOP = DOP_{\max} \frac{\sin^2\gamma_P}{1 + \cos^2\gamma_P}, \tag{11}$$

where γ_P, called the scattering angle, is the angle between observation point P and the sun. $DOP_{\max}$ is the maximum detected DOP in the sky and $DOP_{\max}=1$ for an ideal sky.

The Rayleigh sky model predicts the sky polarization properties AOP[26] as

$$AOP= \arctan\frac{\sin h_S\cos h_P-\cos h_S\sin h_P\cos\left(\varphi_{gS}-\varphi_{gP}\right)}{\sin\left(\varphi_{gS}-\varphi_{gP}\right)\cos h_S}, \tag{12}$$

where h_P is the altitude angle of observation point P, φ_{gP} is the azimuth angle of P in the ENU coordinate, and $AOP\in(-90,90)$. According to trigonometric functions,

$$\begin{cases}\dfrac{\sin AOP}{\cos AOP}=\tan AOP\\ \sin^2 AOP+\cos^2 AOP=1\end{cases}. \tag{13}$$

Then, $\sin AOP$ and $\cos AOP$ are given by

$$\begin{cases}\sin AOP=\dfrac{\sin h_S\cos h_P-\cos h_S\sin h_P\cos\left(\varphi_{gS}-\varphi_{gP}\right)}{\sin\gamma_P}\\ \cos AOP=\dfrac{\sin\left(\varphi_{gS}-\varphi_{gP}\right)}{\sin\gamma_P}\cos h_S\end{cases}. \tag{14}$$

The sky polarization E-vector in the ENU coordinate predicted by the Rayleigh sky model is given as

$$\boldsymbol{E}_{gP}=\boldsymbol{V}_{gP}\cos AOP+\boldsymbol{H}_{gP}\sin AOP, \tag{15}$$

where $\boldsymbol{E}_{gP}$ is the polarization E-vector of observation point P in the ENU coordinate predicted, $\boldsymbol{V}_{gP}$ is the tangent direction of the local meridian, and $\boldsymbol{H}_{gP}$ is the vector perpendicular to $\boldsymbol{V}_{gP}$ and parallel to the ox_gy_g plane. $\boldsymbol{V}_{gP}\cos AOP$ and $\boldsymbol{H}_{gP}\sin AOP$ are the projections of the polarization E-vector on $\boldsymbol{V}_{gP}$ and $\boldsymbol{H}_{gP}$, respectively:

$$\boldsymbol{V}_{gP}=(-\sin h_P\sin\varphi_{gP},-\sin h_P\cos\varphi_{gP},\cos h_P)^{\mathrm{T}}, \tag{16}$$

$$\boldsymbol{H}_{gP}=(-\cos\varphi_{gP},\sin\varphi_{gP},0)^{\mathrm{T}}. \tag{17}$$

The superscript T represents a matrix or a vector transpose. Substituting (14) into (15), $\boldsymbol{E}_{gP}$ in the ENU coordinate is given as

$$\boldsymbol{E}_{gP}=\begin{bmatrix}\dfrac{\cos\varphi_{gS}\sin h_P\cos h_S-\cos\varphi_{gP}\cos h_P\sin h_S}{\sin\gamma_P}\\ \dfrac{-\sin\varphi_{gS}\sin h_P\cos h_S+\sin\varphi_{gP}\cos h_P\sin h_S}{\sin\gamma_P}\\ \dfrac{\sin(\varphi_{gS}-\varphi_{gP})\cos h_S\cos h_P}{\sin\gamma_P}\end{bmatrix}. \tag{18}$$

In short, the polarization E-vector $\boldsymbol{E}_{aP}$ in the sun azimuth coordinate can be expressed as

$$\boldsymbol{E}_{aP}=C_g^a\boldsymbol{E}_{gP}. \tag{19}$$

2.3 Hypothetical polarization imager

To construct an ideal simulation system, both the skylight polarization model and the polarization imaging sensor must be constructed [37]. In this section, a hypothetical polarization imager is designed and described in detail.

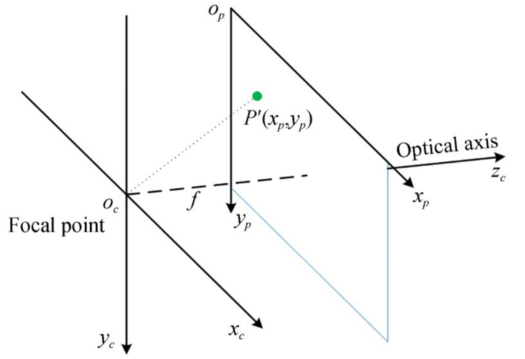

Fig. 4 Camera coordinate frame $o_cx_cy_cz_c$ and pixel coordinate frame $o_px_py_p$, where f is focal length

To construct a hypothetical polarization imager, camera and pixel coordinate frames were established, as depicted in Fig. 4. The z_c axis of the camera coordinate frame $o_cx_cy_cz_c$ was aligned with the optical axis of the imager, and the x_c and y_c axes of the camera coordinate frame $o_cx_cy_cz_c$ were aligned with the column and row directions of the image, respectively. The x_p and y_p axes of the pixel coordinate frame $o_px_py_p$ were aligned with the column and row directions of the image, respectively. The unit of this coordinate is pixels.

In the camera coordinate frame, the vector of pixel $P'(x_{pP'}, y_{pP'})$ is

$$\boldsymbol{V}_{cP'}=D\left[_x\left(x_{pP'}-\frac{\eta_x+1}{2}\right), D_y\left(y_{pP'}-\frac{\eta_y+1}{2}\right), f\right]^{\mathrm{T}}, \tag{20}$$

where D_x and D_y are the column and row pixel sizes, respectively, η_x and η_y indicate that the polarization image has $\eta_x \times \eta_y$ pixels, and f is the focal length of the pixel-based polarization camera used.

Suppose three Euler angles of the polarization imager are given. Then the rotation matrix from the camera coordinate to the sun azimuth coordinate can be described as

$$C_c^a=\begin{bmatrix} \cos\beta\cos\psi+\sin\beta\sin\alpha\sin\psi & \cos\alpha\sin\psi & \sin\beta\cos\psi-\cos\beta\sin\alpha\sin\psi \\ -\cos\beta\sin\psi+\sin\beta\sin\alpha\cos\psi & \cos\alpha\cos\psi & -\sin\beta\sin\psi-\cos\beta\sin\alpha\cos\psi \\ -\sin\beta\cos\alpha & \sin\alpha & \cos\beta\cos\alpha \end{bmatrix}, \tag{21}$$

where ψ, α, and β represent the yaw, pitch, and roll angle, respectively.

Then, the shooting direction of pixel P' in the sun azimuth coordinate is

$$\boldsymbol{V}_{aP'}=C_c^a\boldsymbol{V}_{cP'}. \tag{22}$$

Azimuth angle $\varphi_{aP'}$ of the shooting direction of pixel P' in the sun azimuth coordinate is

$$\varphi_{aP'}=\arctan\left[\frac{\boldsymbol{V}_{aP'}(1,1)}{\boldsymbol{V}_{aP'}(2,1)}\right]. \tag{23}$$

Altitude angle $h_{P'}$ of the shooting direction of pixel P' is

$$h_{P'}=\arcsin\left[\frac{\boldsymbol{V}_{aP'}(3,1)}{\left|\boldsymbol{V}_{aP'}\right|}\right], \tag{24}$$

where $\boldsymbol{V}_{aP'}(1,1)$, $\boldsymbol{V}_{aP'}(2,1)$, and $\boldsymbol{V}_{aP'}(3,1)$ are the components of $\boldsymbol{V}_{aP'}$, and $\left|\boldsymbol{V}_{aP'}\right|$ is the mode of $\boldsymbol{V}_{aP'}$. Then, the scattering angle $\gamma_{P'}$ of the pixel P' is given as

$$\gamma_{P'}=\arccos\left[\sin h_{P'}\sin h_S+\cos h_{P'}\cos h_S\cos(\varphi_{aP'})\right]. \tag{25}$$

Substituting Eq. (25) into Eq. (11), the DOP of pixel P' can be obtained. Fig. 5(a) depicts a hypothetical DOP image.

The azimuth angle $\varphi_{gP'}$ of the shooting direction of pixel P' in the ENU coordinate is

$$\varphi_{gP'}=\varphi_{aP'}-\varphi_{gS}. \tag{26}$$

Therefore, substituting Eqs. (24), (26), and (18) into Eq. (19), the polarization E-vector $\boldsymbol{E}_{aP'}$ of pixel P' in the sun azimuth coordinate frame can be obtained. The polarization E-vector $\boldsymbol{E}_{cP'}$ of P' in the camera coordinate frame can be given by

$$\boldsymbol{E}_{cP'}=C_a^c\boldsymbol{E}_{aP'}, \tag{27}$$

where C_a^c is the transpose of C_c^a, which represents the rotation matrix from the sun azimuth coordinate to the camera coordinate. Because the AOP reference direction is aligned with the y_b axis and the shooting direction of the hypothetical polarization imager is aligned with the z_c axis, the AOP can be calculated as

$$AOP=\arctan\frac{\boldsymbol{E}_{cP'}(1,1)}{\boldsymbol{E}_{cP'}(2,1)}, \tag{28}$$

where $\boldsymbol{E}_{cP'}(1,1)$ and $\boldsymbol{E}_{cP'}(2,1)$ are the components of $\boldsymbol{E}_{cP'}$. A hypothetical AOP image is depicted in Fig. 5(b).

For the four typical orientation-determination algorithms described in Section 1, the zenith and least-squares approaches can directly use the AOP for orientation determination. However, for the SM-ASM and symmetry approaches, further transformation of AOP is required. The reference direction of AOP must be converted to the local meridian. The AOP whose reference direction is local meridian can be defined as

$$AOPLM=AOP-\xi, \tag{29}$$

where ξ is the angle between the y_c axis and the local meridian. When the polarization imager points to the sky zenith, we have

$$\xi=\arctan\left[\frac{\left(x_{pP'}-\dfrac{\eta_x+1}{2}\right)}{\left(y_{pP'}-\dfrac{\eta_y+1}{2}\right)}\right]. \tag{30}$$

A hypothetical AOPLM image is obtained and depicted in Fig. 5(c).

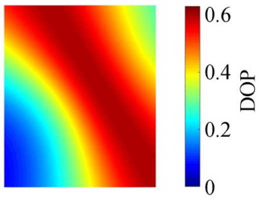

(a) DOP image

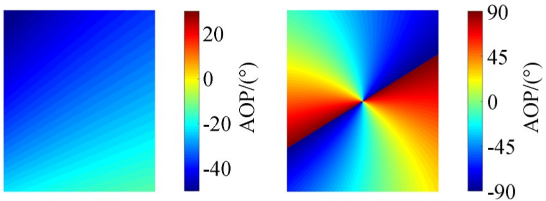

(b) AOP image (c) AOPLM image

Fig. 5 Hypothetical polarization images

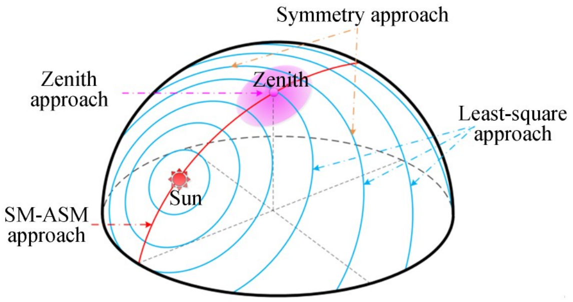

Fig. 6 Rayleigh sky model and four typical orientation-determination approaches (The red dot represents the sun, the pink point represents the sky zenith, red line represents the solar meridian and anti-solar meridian (SM-ASM), blue lines represent the polarization electric field vectors (*E*-vector))

3 Simulation

To investigate the impact of the sensor tilt on orientation determination, we performed some simulation experiments for four classical polarization-orientation-determination algorithms, namely, the zenith, SM-ASM, symmetry, and least-squares approaches, as depicted in Fig. 6. According to the Rayleigh sky model, the polarization *E*-vector at the sky zenith is perpendicular to the solar azimuth; therefore, the zenith approach determines the heading angle by measuring the AOP at the sky zenith [3,16,23-25]. The polarization E-vector along the SM-ASM is always perpendicular to SM-ASM. Therefore, the SM-ASM approach can be used to calculate the heading angle by extracting SM-ASM [26-29]. Using the symmetry of the skylight polarization pattern, the symmetry approach can determine the orientation by symmetry detection [30-32]. The polarization *E*-vector of the Rayleigh sky model is always perpendicular to the solar vector; therefore, the least-squares approach can be used to determine the orientation by the total least square of the polarization *E*-vectors [33-35].

Considering that the polarization imager needs to capture the skylight polarization pattern, the imager field of view must always be above the horizon, and the interference of buildings and obstacles must be eliminated. In our simulation and experiment, the imager angle of view was 108°; therefore, we set the pitch and roll angles to $|\alpha|+|\beta|\leqslant 30°$.

Tab. 1 Simulation parameters

Symbol	Value	Unit	Description
$DOP_{\max}$	1	/	Maximum DOP in the sky
D_x	3.45	μm	Pixel size in column direction
D_y	3.45	μm	Pixel size in row direction
η_x	2048	pixel	Number of pixels in column direction
η_y	2448	pixel	Number of pixels in row direction
f	4	mm	Focal length of polarization imager

The tilt state of the sensor in practice can be divided into three situations:

1) Pitch-tilt-only condition

2) Roll-tilt-only condition

3) Pitch-and-roll-tilt condition

The parameters of the simulation are listed in Tab. 1.

3.1 Pitch-tilt-only condition

In this section, we discuss the error characteristics of the pitch-angle-only condition with the roll angle set to zero. Using the polarization compass simulation system discussed in Section 2, more than 1.4×10^5 sets of simulation experiments were performed, and the orientation errors of four typical approaches were obtained in the ranges of solar altitude angle $h_S \in [0°, 50°]$, yaw angle $\psi \in [-180°, 180°]$, pitch angle, $\alpha \in [-30°, 30°]$, and roll angle $\beta = 0°$. The results of the pitch-tilt-only condition are depicted in Fig. 7.

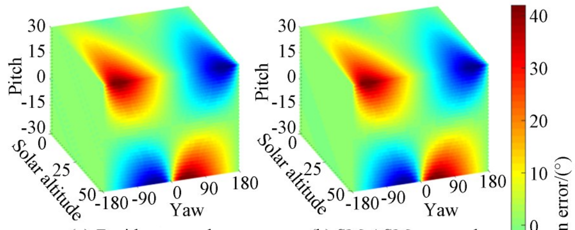

(a) Zenith approach　(b) SM-ASM approach

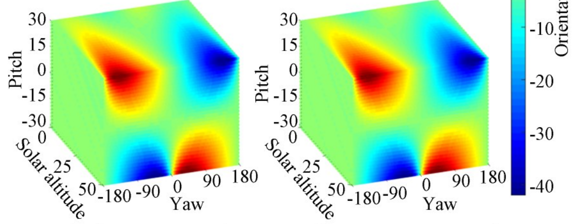

(c) Symmetry aproach　(d)Least-square approach

Fig. 7　Orientation errors of four typical polarization-orientation-determination approaches under pitch tilt

It can be observed in Fig. 7 that under the pitch-tilt-only condition, the variation trend of the orientation error for the four typical approaches is the same. There were three similarities:

(a) When the pitch angle was 0°, the error in all four approaches was close to 0. With an increase in the pitch angle, the error tended to increase.

(b) When the solar altitude angle was 0°, the error in all the four approaches was always close to 0°. When the pitch angle was not 0°, the error in all approaches tended to increase with an increase in the solar altitude angle.

(c) The error in the four approaches is symmetric with respect to planes $\psi = 0°$ and $\psi = 180°$ $(-180°)$. When the yaw angle was 0° or 180°(−180°), regardless of the pitch and solar altitude angles, the error in all the four typical approaches were always close to zero. In addition, the following trends were observed: error was close to zero at $\psi = -180°$. With the yaw angle increasing gradually, the error increased gradually and reached a maximum before the error decreased and approached zero at $\psi = 0°$. Subsequently, with the yaw angle increasing gradually, the orientation calculating error increased gradually and reached a maximum. Finally, the orientation error decreased and was close to zero at $\psi = 180°$.

The following is a detailed analysis of the reasons for the above three similarities:

For (a), when $\alpha = 0°$, there is no impact of the sensor tilt. In other words, under ideal conditions, all four typical approaches can effectively determine the orientation. When the pitch tilt increases, the tilt interference increases, which leads to an increase in orientation-determination errors.

For (b), the four approaches essentially use the solar azimuth information to determine the orientation. When the solar altitude angle increases, the component of the solar vector projected on the plane $ox_a y_a$ $(ox_g y_g)$ decreases, thus the stability and reliability of the solar azimuth are weakened. This causes an increase in orientation-determination errors.

For (c), the errors in the four approaches are all symmetric with respect to planes $\psi = 0°$ and $\psi = 180°(-180°)$. This manifests in the symmetry of the skylight polarization pattern with respect to SM-ASM. When the yaw angle is 0° or 180° (−180°) and only pitch tilt occurs, the direction of the polarization imager′s optical axis always points to SM-ASM, which is parallel to the y_c axis. Therefore, when the yaw angle is 0° or 180° (−180°), regardless of the pitch and solar altitude angles, the errors in the four approaches are always close to zero.

To further compare these four approaches, we drew groups of simulation results of the four approaches on a graph, as depicted in Figs. 8 and 9. It is evident that the variation trends of the four error curves are identical, and the four curves almost coincide. Furthermore, under similar conditions, the error difference between these four approaches is always less than 0.66°. Therefore, when there is interference from only the pitch tilt, it can be concluded that the error characteristics of the four approaches are consistent, and the orientation errors of the four approaches are almost the same. Moreover, similarity (b) is evident in Fig. 8, and similarities (a) and (c) can be partially reflected in Fig. 9.

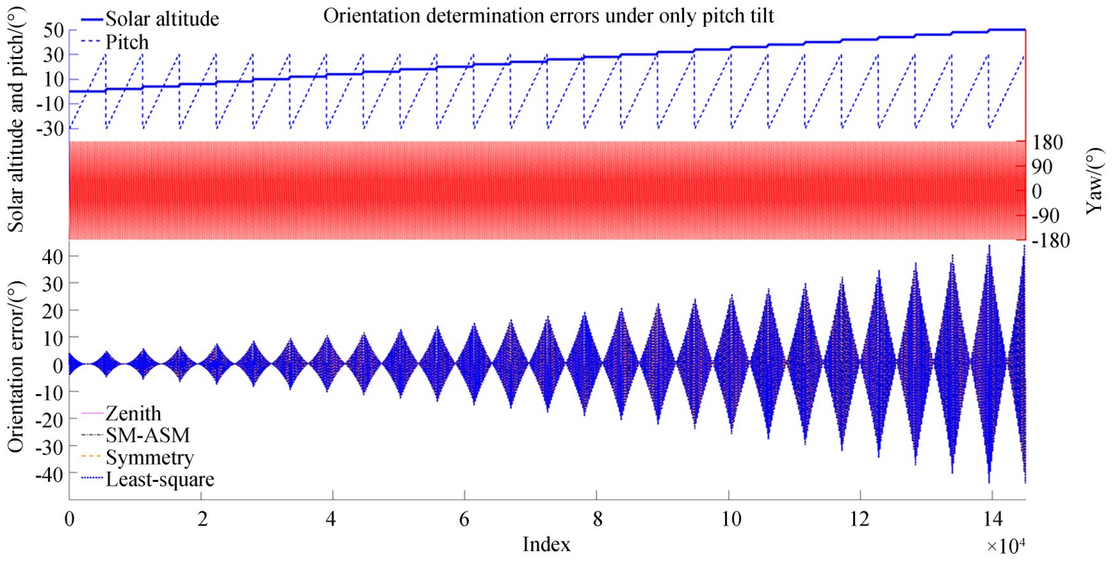

Fig. 8 Simulated orientation-determination error curves of four typical polarization-orientation-determination approaches under the pitch-tilt-only condition

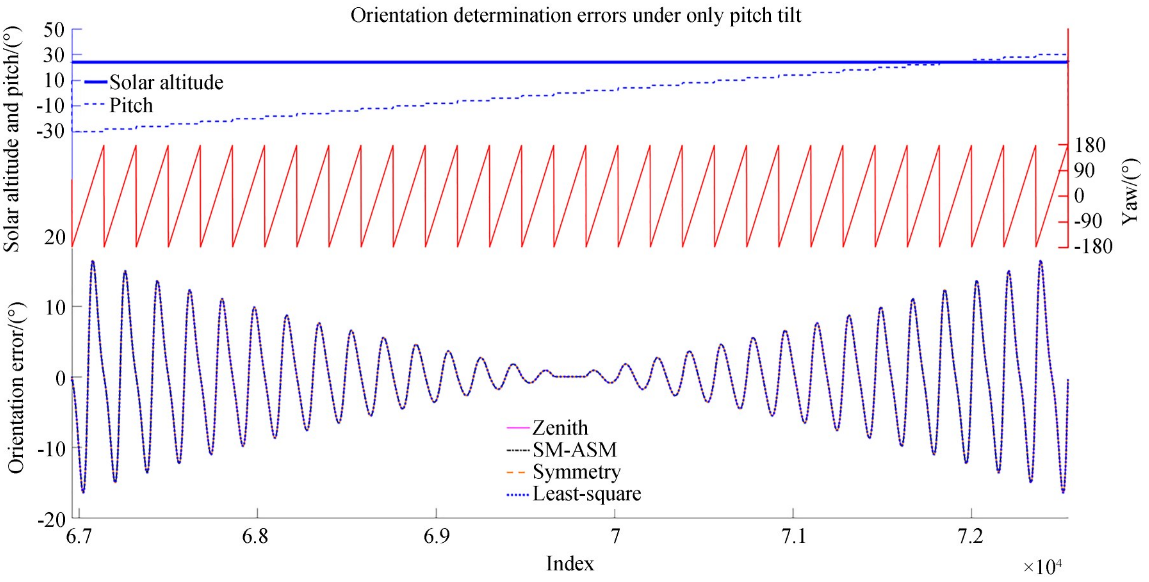

Fig. 9 Simulated orientation-determination error curves of four typical approaches under the pitch-tilt-only situation. This is an enlarged view of Fig. 8

3.2 Roll-tilt-only condition

In this section, we discuss the error characteristics for the situations when only the roll angle tilt exists and with the pitch angle set to zero. The orientation errors in four typical approaches were obtained in the ranges of the solar altitude angle $h_S \in [0°, 50°]$, yaw angle $\psi \in [-180°, 180°]$, roll angle, $\beta \in [-30°, 30°]$, and pitch angle $\alpha = 0°$.

The results under this condition are depicted in Fig. 10, where the yaw range is [$-180°, 180°$]. For ease of observation and comparison, the range of yaw is converted to [$-90°, 270°$], as depicted in Fig. 11. By comparing Figs. 11 and 7, it is evident that the two sets of graphs have identical shapes, with the only difference being the range of the yaw angle. Therefore, the error characteristics of the roll-tilt-only condition are significantly similar to those of the pitch-tilt-only condition. The first two error similarities are the same as those described in Section 3.1; however, the third one is different.

For only roll tilt, the errors in the four approaches were all symmetric with respect to planes$\psi = -90°(270°)$ and $\psi = 90°$. When the yaw angle was 90° or $-90°(270°)$, regardless of the roll and solar altitude angles, the errors of the four typical approaches were always close to zero. We observed the following trends: the error was close to zero at $\psi = -90°$, and with the yaw angle increasing gradually, the error increased gradually and reached a maximum. Subsequently, the error decreased and was close to zero at $\psi = 90°$. Then, as the yaw angle increased gradually, the error increased gradually and reached a maximum. Finally, the error decreased and was close to zero at $\psi = 270°$.

In short, compared with the result of the pitch-tilt-only condition, the result of the roll-tilt-only case has a 90° shift in the yaw direction. The reason for this phenomenon is given in below.

As depicted in Fig. 4, the direction of the optical axis of the polarization imager is $(0, 0, 1)^{\mathrm{T}}$. Using Eq. (22), the optical axis direction in the sun azimuth coordinate is given by

$$\boldsymbol{V}_{af} = C_c^a \begin{pmatrix} 0 \\ 0 \\ 1 \end{pmatrix} = \begin{pmatrix} \sin\beta\cos\psi - \cos\beta\sin\alpha\sin\psi \\ -\sin\beta\sin\psi - \cos\beta\sin\alpha\cos\psi \\ \cos\beta\cos\alpha \end{pmatrix}. \tag{31}$$

Assume two sets of altitudes $(\psi_1, \alpha_1, \beta_1)$ and $(\psi_2, \alpha_2, \beta_2)$ that satisfy $\psi_2 = \psi_1 + 90°$, $\beta_2 = \alpha_1$, $\beta_1 = 0°$, and $\alpha_2 = 0°$.

$$\boldsymbol{V}_{af1} = \begin{pmatrix} \sin\beta_1\cos\psi_1 - \cos\beta_1\sin\alpha_1\sin\psi_1 \\ -\sin\beta_1\sin\psi_1 - \cos\beta_1\sin\alpha_1\cos\psi_1 \\ \cos\beta_1\cos\alpha_1 \end{pmatrix} = \begin{pmatrix} -\sin\alpha_1\sin\psi_1 \\ -\sin\alpha_1\cos\psi_1 \\ \cos\alpha_1 \end{pmatrix} = \begin{pmatrix} \sin\beta_2\cos\psi_2 \\ -\sin\beta_2\sin\psi_2 \\ \cos\beta_2 \end{pmatrix} =$$
$$\begin{pmatrix} \sin\beta_2\cos\psi_2 - \cos\beta_2\sin\alpha_2\sin\psi_2 \\ -\sin\beta_2\sin\psi_2 - \cos\beta_2\sin\alpha_2\cos\psi_2 \\ \cos\beta_2\cos\alpha_2 \end{pmatrix} = \boldsymbol{V}_{af2}, \tag{32}$$

where $\boldsymbol{V}_{af1}$ and $\boldsymbol{V}_{af2}$ are the optical axis directions at $(\psi_1, \alpha_1, \beta_1)$ and $(\psi_2, \alpha_2, \beta_2)$ in the sun azimuth coordinate system, respectively. $\boldsymbol{V}_{af1} = \boldsymbol{V}_{af2}$ indicates that the optical axis directions of the image at $(\psi_1, \alpha_1, \beta_1)$ and $(\psi_2, \alpha_2, \beta_2)$ are identical. Therefore, the polarization information collected by the polarization imager at $(\psi_1, \alpha_1, \beta_1)$ and $(\psi_2, \alpha_2, \beta_2)$ corresponds to almost the same area of the sky. As such, the results of the roll-tilt-only condition have a 90° shift in the yaw direction compared with that of the pitch-tilt-only condition.

To further compare these four approaches under the roll-tilt-only condition, we obtained groups of simulation results of the four approaches on a graph, as depicted in Figs. 12 and 13. It is evident that the variation trends of the four error curves are identical, and the four curves almost coincide. Furthermore, as depicted in Fig. 13, the error curve of the pitch-tilt-only condition is drawn for comparison with that of the roll-tilt-only condition. It is evident that the results of the roll-tilt-only condition have a 90° shift in the yaw direction

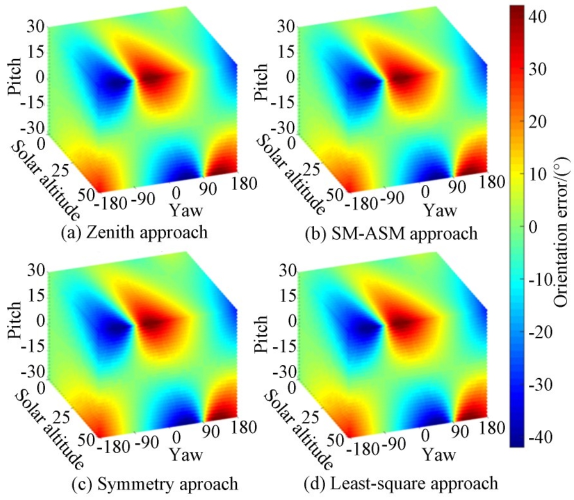

(a) Zenith approach (b) SM-ASM approach

(c) Symmetry aproach (d) Least-square approach

Fig. 10 Orientation-determination errors in four typical polarization-orientation-determination approaches under the roll-tilt-only condition with $\psi\in[-180°, 180°]$

compared with that of the pitch-tilt-only condition. Therefore, the properties of the roll-tilt-only condition can be obtained from that of the pitch-tilt-only condition.

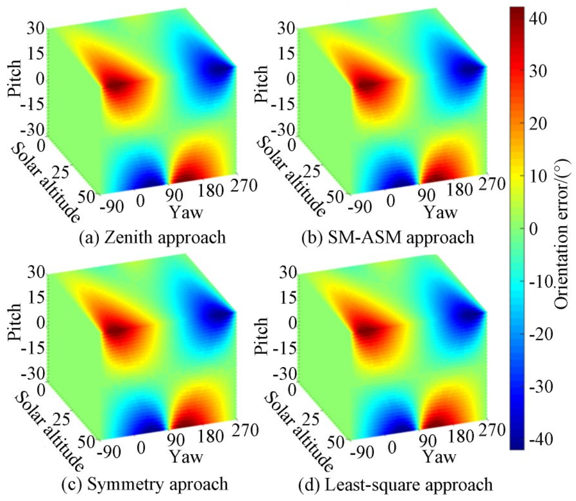

(a) Zenith approach (b) SM-ASM approach

(c) Symmetry aproach (d) Least-square approach

Fig. 11 Orientation-determination errors in four typical polarization-orientation-determination approaches under the roll-tilt-only condition with $\psi\in[-90°, 270°]$

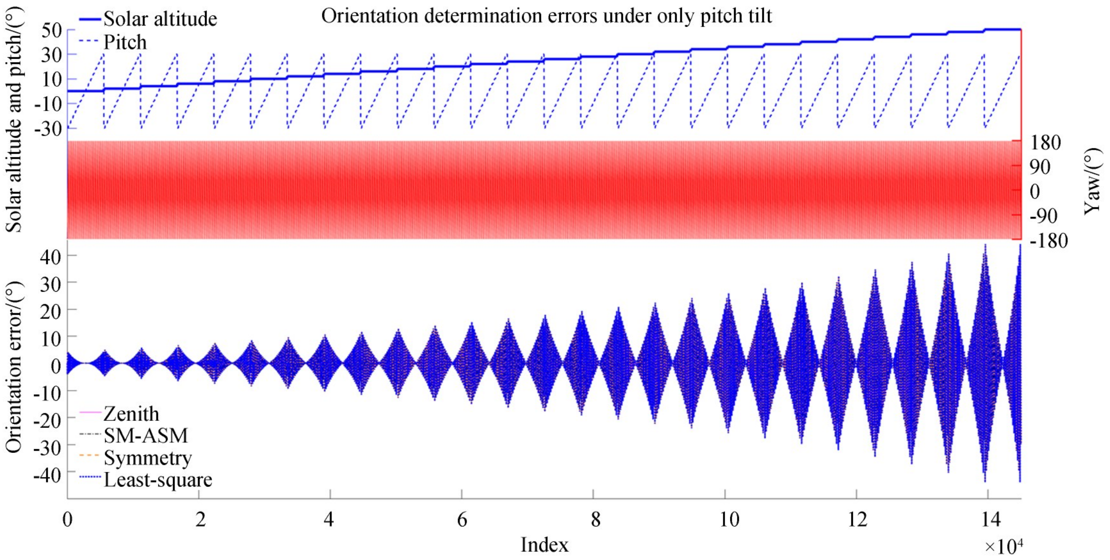

Fig. 12 Simulated orientation-determination error curves of four typical polarization-orientation-determination approaches under the roll tilt only situation

3.3 Pitch-and-roll-tilt condition

The error characteristics of the pitch-and-roll-tilt condition are discussed in this section. The orientation-determination errors of four typical approaches were obtained in the ranges of the solar altitude angle $h_S\in[0°, 50°]$, yaw angle $\psi\in[-180°, 180°]$, pitch angle $\alpha\in[-30°, 30°]$, roll angle, $\beta\in[-30°, 30°]$, and $|\alpha|+|\beta|\leqslant 30°$. The results of the zenith approach for pitch and roll tilts are depicted in Fig. 14.

It is evident from Fig. 14 that under the pitch-and-roll-tilt condition the error in the zenith

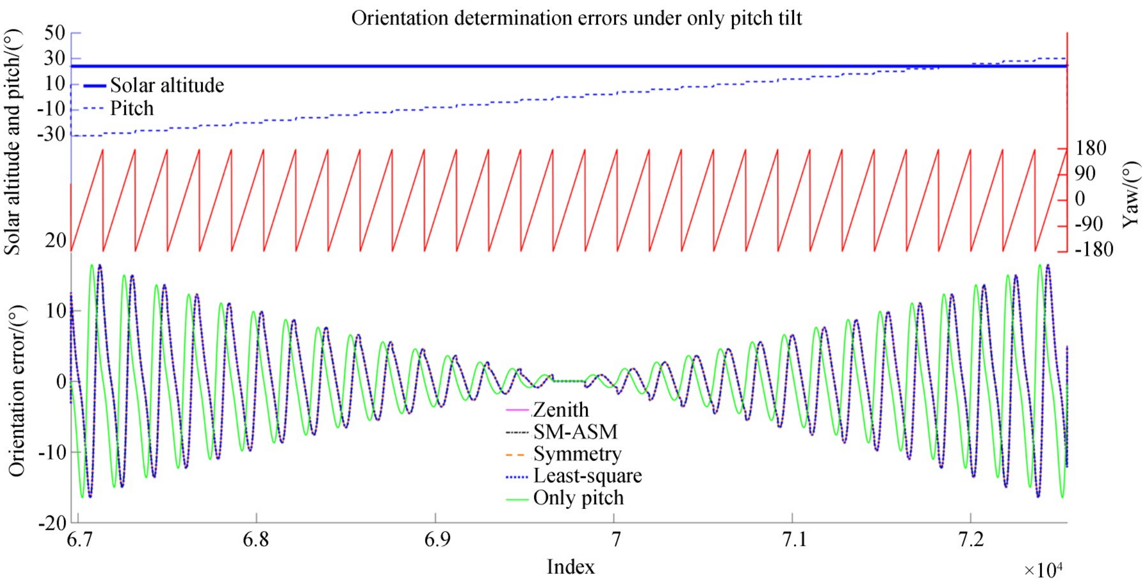

Fig. 13 Simulated orientation-determination error curves of four typical approaches under the roll tilt only situation. This is an enlarged view of Fig. 12. Only pitch is the error curve when the pitch angle equals the roll angle under the pitch-tilt-only situation

approach has the following characteristics:

(a) With an increase in pitch and roll angles, the error in the zenith approach tends to increase.

(b) When the solar altitude angle was 0°, the orientation error in the zenith approach was close to 0°. When the pitch and roll angles were not 0°, the error tended to increase with an increase in the solar altitude angle.

(c) When the other conditions were the same, the yaw angle difference also affected the orientation errors.

The reasons for these observations are identical to those mentioned in Section 3.1. The following is a detailed analysis of the reasons for these three characteristics.

For (a), when the pitch and roll tilts increase, the tilt interference increases, which leads to an increase in orientation errors.

For (b), the zenith approach essentially uses solar azimuth information to determine the orientation. When the solar altitude angle increases, the component of the solar vector projected on the plane $ox_a y_a$ ($ox_g y_g$)decreases, thereby weakening the stability and reliability of the solar azimuth. This leads to an increase in the orientation error.

For (c), with different yaw angles, the relative position between the sun and the polarization sensor is different, resulting in different orientation errors when the sensor tilts.

Under pitch and roll tilts, the error difference between the four approaches was always less than 0.77°. Therefore, the error characteristics of the other three approaches were consistent with those of the zenith approach.

3.4 Application values

The findings of this study have two important application: (1) Given the allowable error range of the orientation, the allowable range of the corresponding pitch and roll angles can be obtained. (2) The error caused by the sensor tilt can be corrected when the pitch angle and roll angle are given.

The allowable ranges of the pitch and roll angles are illustrated by considering the allowable maximum error of orientation as an example. Suppose that the maximum allowable error of orientation is ME. It is important to note that for any yaw angle, the maximum error of orientation is affected not only by the pitch and roll angles but also by the solar altitude angle. When the pitch and roll angles are 0°, the orientation-determination er-

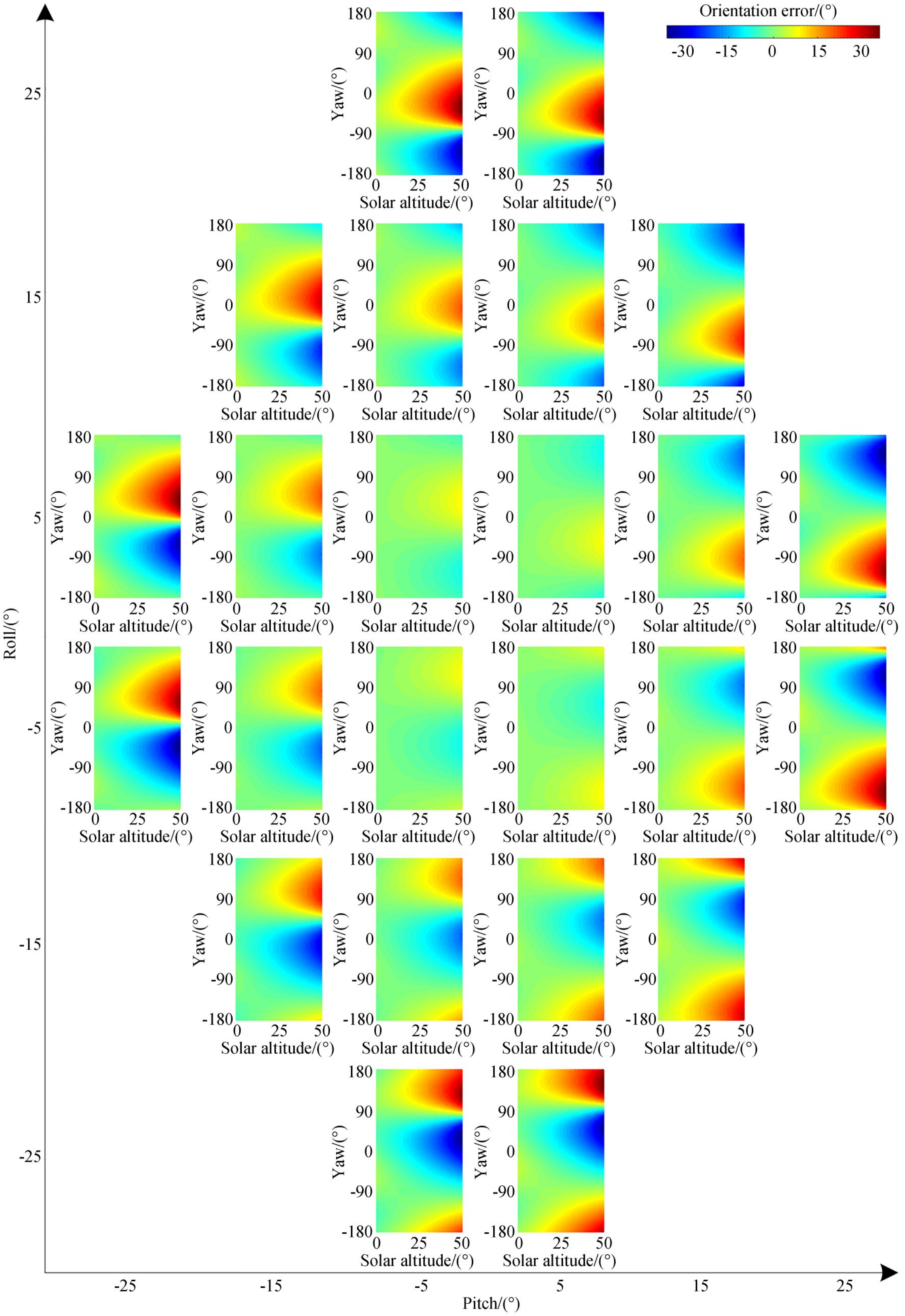

Fig. 14　Simulated orientation-determination error of the zenith approach under the pitch-and-roll-tilt condition

ror caused by the sensor tilt is 0°. When the pitch or roll angle increases, the maximum error in the orientation determination increases. When the solar altitude angle is 0°, the orientation-determination error is almost unaffected by the sensor tilt. When the solar altitude angle increases, the maximum error of the orientation determination increases. Based on the simulation results, the allowable ranges of the pitch and roll angles can be roughly estimated by

$$h_S\sqrt{\alpha^2+\beta^2}\leqslant ME^2. \tag{33}$$

The results of this study can mitigate such orientation-determination errors. The impact of the sensor tilt is a type of system error, and a method of eliminating this error is to fully analyze its characteristics. Therefore, given the pitch angle and roll angle, the error caused by the tilt can be obtained based on the results of this study. Subsequently, the orientation can be calibrated by subtracting this error. In our field experiment, we mitigated such orientation-determination errors, as discussed in Section 4.

4 Field experiment

To further verify the simulation results, field experiments were performed to investigate the impact of the polarization sensor tilt on orientation determination. The results of the field experiments were compared with those of the simulation.

The experimental platform used in this study is depicted in Fig. 15. Two tripods were equipped with a Sony IMX250MZR polarization imager and a GPS/IMU (global position system/inertial measurement units) integrated navigation system. The parameters of the actual polarization imager were consistent with those of the hypothetical polarization imager, as listed in Table 1. The GPS/IMU integrated navigation system was used to determine the pitch and roll angles of the polarization imager. The true North was determined by a double-antenna GPS device as a benchmark (the orientation resolution was 0.1° with a 2 m baseline). Field experiments were performed in Nanjing, China, on the roof of our laboratory (32°0136.4″ N, 118°5111.9″ E), between November 15 and November 19, 2019. Meteorological conditions were stable. Fig. 16 depicts a set of actual polarization images.

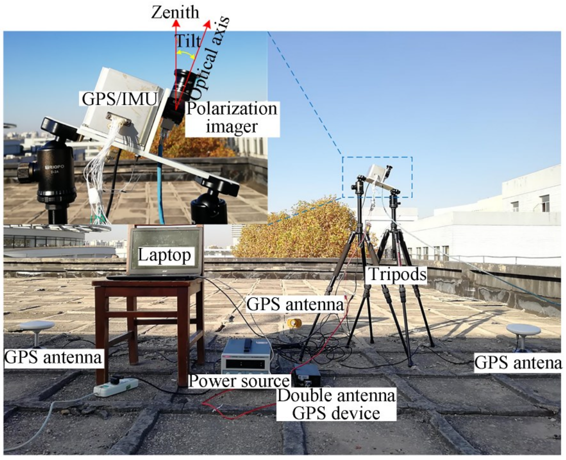

Fig. 15　Polarization-orientation-determination experiment platform

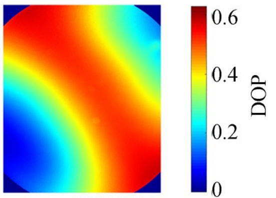

(a) DOP image

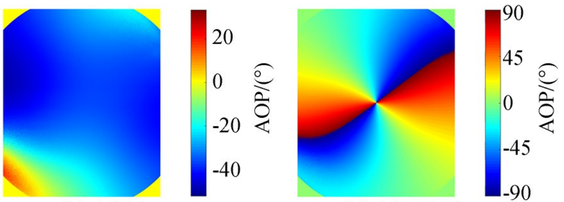

(b) AOP image　(c) AOPLM image

Fig. 16　Actual polarization images (The four corners of these polarization images could not be properly imaged owing to the short focal lens used in the imager. Therefore, these are not used in polarized skylight navigation and are set to 0)

To determine the impact of the sensor tilt, field experiments were performed for the pitch-tilt-only, roll-tilt-only, and pitch-and-roll-tilt conditions. The experimental results are depicted in Figs. 17-19. The green curves in these figures depict the simulation results. As discussed in Section 3, the orientation errors in the simulation results of the four typical approaches were almost identical. Therefore, only one curve is drawn here to facilitate the observation and comparison of the simulation and experimental results. The dithering of the experimental orientation error curves is attributed to cloud interference, which was not the focus of this study.

As is evident in Figs. 17-19 from comparing the simulation results with the experimental results of the four typical approaches, it is clear that: (a) There are some differences between the simulation results and the field experimental results. However, these differences are always within a narrow range. (b) The experimental error curves and simulation error curves have the same variation trend, and the experimental errors in the four typical approaches have the same variation trend.

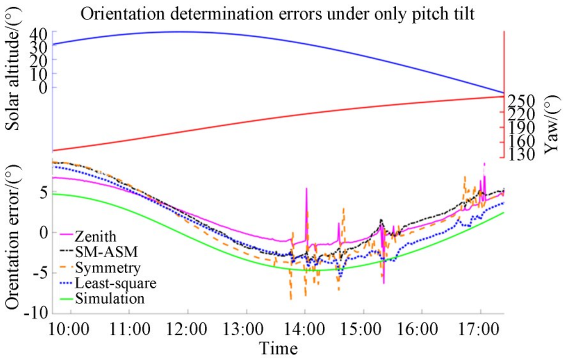

Fig. 17　Field experiment for the pitch-tilt-only condition on 15 November 2019 with pitch angle of −20.0°

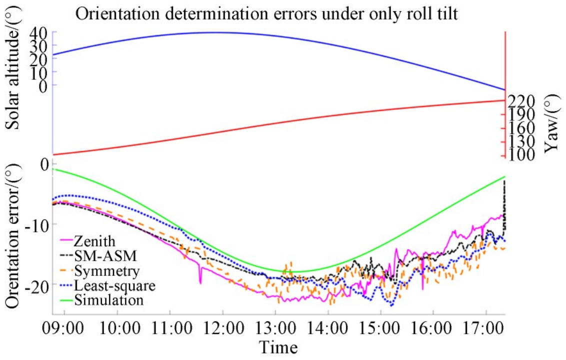

Fig. 18　Field experiment for the roll-tilt-only condition on 16 November 2019 with roll angle of 29.1°

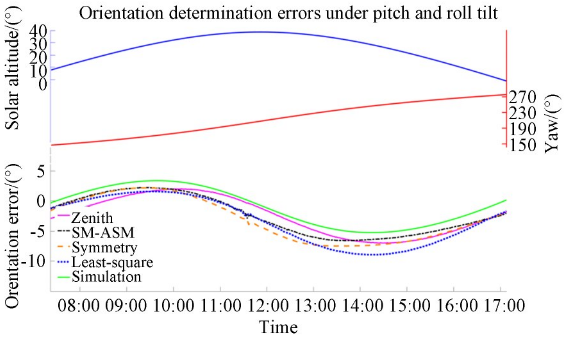

Fig. 19　Field experiment for the pitch-and-roll-tilt condition on 19 November 2019 with pitch and roll angles of −16.3° and −9.9°, respectively

For further analysis, in (a) of the above paragraph, the Rayleigh sky model is an ideal model that only considers a single scattering event and has some differences from the actual skylight polarization pattern[44]. Therefore, the experimental error curves did not coincide with the simulation error curves.

For (b) of the above paragraph, for all the pitch-tilt-only, roll-tilt-only, and pitch-and-roll-tilt conditions, the orientation error curves of the field experiments and simulation had the same variation, and the experimental errors in the four typical approaches had the same variation trend. These results further indicate that the orientation error characteristics of the four typical approaches are consistent under the tilt interference. The simulation error curves of the four typical approaches almost coincided. However, the field experiment error curves of the four typical approaches did not coincide because field experiments were affected by not only sensor tilts but some other disturbances as well, such as measurement noise and clouds. In particular, where the curve wobbles markedly, orientation determination was disturbed by clouds.

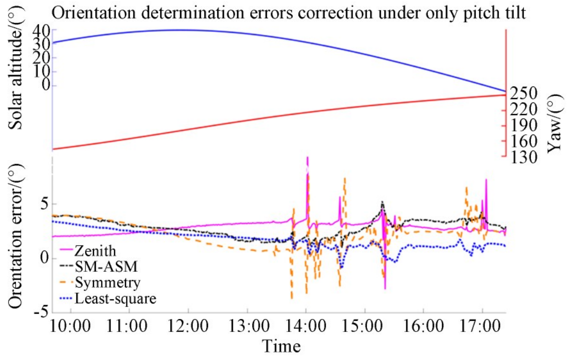

Fig. 20　Orientation-determination error correction for the pitch-tilt-only condition on 15 November 2019 with pitch angle of −20.0°

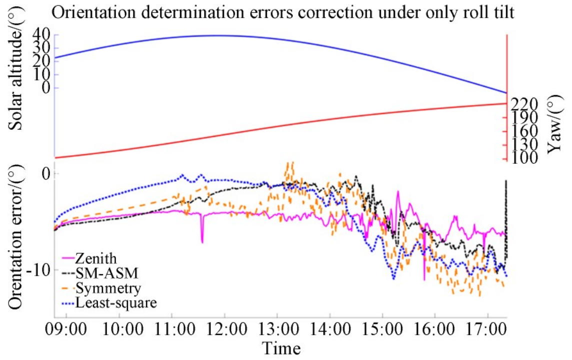

Fig. 21　Orientation-determination error correction for the roll-tilt-only condition on 16 November 2019 with roll angle of 29.1°

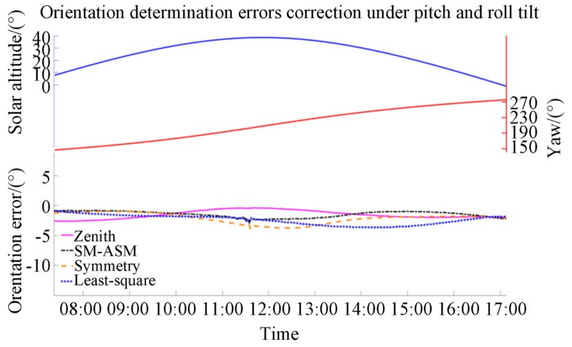

Fig. 22　Orientation-determination error correction for the pitch-and-roll-tilt condition on 19 November 2019 with pitch and roll angles of −16.3° and −9.9°, respectively

As depicted in Figs. 20-22, the results of this study can be used to correct the orientation-determination errors caused by sensor tilts. In particular, when the weather was good, the error correction result was better, as depicted in Fig. 22. However, when the weather conditions were complex and there was interference from clouds, this had some effect on error correction. However, the effect was negligible, as depicted in Figs. 20 and, particularly, in Fig. 21. This is because, when the weather is clear, skylight polarization patterns are closer to the Rayleigh sky model, and there is less interference from meteorological factors such as clouds. However, when the weather conditions are complex, skylight polarization patterns deviate from the Rayleigh sky model, and there is strong interference from meteorological factors, resulting in a poor correction effect.

4　Conclusion

In this study, the impact of the sensor tilt on polarized skylight orientation determination was investigated in detail. Four typical polarization orientation-determination approaches were described and compared with for three different conditions: the pitch-tilt-only, roll-tilt-only, and pitch-and-roll-tilt condition. Simulations based on the Rayleigh sky model indicated that the error characteristics of the four approaches were completely consistent, and the error curves almost coincided when it was only affected by the sensor tilt. With an increase in the tilt and solar altitude, the orientation errors in the four approaches tended to increase. The orientation errors were also affected by the yaw angle. Field experiments suggested that the errors in the four approaches exhibited the same variation trend. These results provide an important reference for the practical application of polarization orientation determination, particularly for the installation error of the sensor, the tilt of the application platform, and the change in the three-dimensional attitude of the carrier.

The results of this study can also mitigate orientation-determination errors caused by sensor tilts and estimate the allowable ranges of the pitch and roll angles when given the allowable error of orientation determination.

The impact of the sensor tilt was investigated in detail using simulations and experiments. The results indicate that polarization orientation determination is not only affected by the sensor tilt but also by the measurement noise and clouds. Therefore, eliminating these impacts for orientation determination will be the focus of our future research.

References:

[1] BROSSARD M, BARRAU A, BONNABEL S. AI-IMU dead-reckoning[EB/OL]. 2019: arXiv: 1904.06064 [cs. RO]. https://arxiv. org/abs/1904.06064

[2] DE PAULA VERONESE L, BADUE C, AUAT CHEEIN F, *et al*. A single sensor system for mapping in GNSS-denied environments[J]. *Cognitive Systems Research*, 2019, 56: 246-261.

[3] AYCOCK T, LOMPADO A, WOLZ T, *et al*. Passive optical sensing of atmospheric polarization for GPS denied operations[C]. *SPIE Defense + Security. Proc SPIE* 9838, *Sensors and Systems for Space Applications IX*, *Baltimore*, *Maryland*, *USA*. 2016, 9838: 98380Y.

[4] LIU G X, SHI L F. Adaptive algorithm of magnetic heading detection[J]. *Measurement Science and Technology*, 2017, 28(11): 115101.

[5] 褚金奎, 关乐, 李世奇, 等. 大气偏振模式图分布及仿生偏振导航技术[J]. 遥感学报, 2018, 22(6): 969-979.

CHU J K, GUAN L, LI SH Q, *et al*. Atmospheric polarization field pattern distribution and polarization navigation technology[J]. *Journal of Remote Sensing*, 2018, 22(6): 969-979. (in Chinese)

[6] 尤政, 赵开春. 仿生偏振特征感知与导航信息融合的空间态势感知系统[J]. 遥感学报, 22(6): 917-925.

YOU ZH, ZHAO K CH. Space situational awareness system based on bionic polarization feature sensing and navigation information fusion[J]. *Journal of Remote Sensing*, 2018, 22(6):917-925. (in Chinese)

[7] WEHNER R. Desert ant navigation: how miniature brains solve complex tasks[J]. *Journal of Comparative Physiology A*, 2003, 189(8): 579-588.

[8] WINTER C M, BREED M D. Homeward navigation in Pogonomyrmex occidentalis harvester ants [J]. *Insectes Sociaux*, 2017, 64(1): 55-64.

[9] EVANGELISTA C, KRAFT P, DACKE M, *et al*. Honeybee navigation: critically examining the role of the polarization compass[J]. *Philosophical Transactions of the Royal Society B*: *Biological Sciences*, 2014, 369(1636): 20130037.

[10] KRAFT P, EVANGELISTA C, DACKE M, *et al*. Honeybee navigation: following routes using polarized-light cues[J]. *Philos Trans R Soc Lond B Biol Sci*, 2011, 366(1565): 703-708.

[11] MUHEIM R. Behavioural and physiological mechanisms of polarized light sensitivity in birds[J]. *Philosophical Transactions of the Royal Society of London Series B*, *Biological Sciences*, 2011, 366(1565): 763-771.

[12] SCHMELING F, TEGTMEIER J, KINOSHITA M, *et al*. Photoreceptor projections and receptive fields in the dorsal rim area and main retina of the locust eye[J]. *Journal of Comparative Physiology A*, 2015, 201(5): 427-440.

[13] HOMBERG U. Sky compass orientation in desert locusts-evidence from field and laboratory studies [J]. *Front Behav Neurosci*, 2015, 9: 346.

[14] HORVÁTH G. *Polarized Light and Polarization Vision in Animal Sciences* [M]. Berlin, Heidelberg: Springer Berlin Heidelberg, 2014.

[15] GKANIAS E, RISSE B, MANGAN M, *et al*. From skylight input to behavioural output: a computational model of the insect polarised light compass[J]. *PLoS Computational Biology*, 2019, 15(7): e1007123.

[16] AYCOCK T M, LOMPADO A, WHEELER B M. Using atmospheric polarization patterns for azimuth sensing[C]. *SPIE Defense + Security. Proc SPIE* 9085, *Sensors and Systems for Space Applications VII*, *Baltimore*, *Maryland*, *USA*. 2014, 9085: 90850B.

[17] BOHREN C F. *Atmospheric Optics* [M]. Pennsylvania Pennsylvania State University, 2007.

[18] KOKHANOVSKY A A. *Light Scattering Reviews* 10[M]. Berlin, Heidelberg: Springer Berlin Heidelberg, 2016.

[19] CHENG H Y, CHU J K, ZHANG R, *et al.* Underwater polarization patterns considering single Rayleigh scattering of water molecules[J]. *International Journal of Remote Sensing*, 2020, 41(13): 4947-4962.

[20] POMOZI I, HORVÁTH G, WEHNER R. How the clear-sky angle of polarization pattern continues underneath clouds: full-sky measurements and implications for animal orientation[J]. *The Journal of Experimental Biology*, 2001, 204(Pt 17): 2933-2942.

[21] SUHAI B C, HORVÁTH G. How well does the Rayleigh model describe the E-vector distribution of skylight in clear and cloudy conditions? A full-sky polarimetric study[J]. *Josa A*, 2004, 21(9): 1669-1676.

[22] RAYLEIGH L. On the scattering of light by small particles[J]. *Philosophical Magazine*, 1871, 41(275): 447-454.

[23] DUPEYROUX J, SERRES J R, VIOLLET S. AntBot: a six-legged walking robot able to home like desert ants in outdoor environments[J]. *Science Robotics*, 2019, 4(27): eaau0307.

[24] DUPEYROUX J, VIOLLET S, SERRES J R. An ant-inspired celestial compass applied to autonomous outdoor robot navigation[J]. *Robotics and Autonomous Systems*, 2019, 117: 40-56.

[25] DUPEYROUX J, VIOLLET S, SERRES J R. Polarized skylight-based heading measurements: a bio-inspired approach[J]. *Journal of the Royal Society, Interface*, 2019, 16(150): 20180878.

[26] LU H, ZHAO K C, YOU Z, et al. Angle algorithm based on Hough transform for imaging polarization navigation sensor [J]. *Optics Express*, 2015, 23(6): 7248-7262.

[27] TANG J, ZHANG N, LI D L, *et al.* Novel robust skylight compass method based on full-sky polarization imaging under harsh conditions[J]. *Optics Express*, 2016, 24(14): 15834-15844.

[28] LU H, ZHAO K C, WANG X C, *et al.* Real-time imaging orientation determination system to verify imaging polarization navigation algorithm [J]. *Sensors* (*Basel*, *Switzerland*), 2016, 16(2): 144.

[29] GUAN L, LI S Q, ZHAI L Y, et al. Study on skylight polarization patterns over the ocean for polarized light navigation application[J]. *Applied Optics*, 2018, 57(21): 6243-6251.

[30] ZHANG W J, CAO Y, ZHANG X Z, et al. Angle of sky light polarization derived from digital images of the sky under various conditions[J]. *Applied Optics*, 2017, 56(3): 587-595.

[31] MA T, HU X, ZHANG L, et al. An evaluation of skylight polarization patterns for navigation[J]. *Sensors* (*Basel*), 2015, 15(3): 5895-5913.

[32] ZHAO H J, XU W J, ZHANG Y, *et al.* Polarization patterns under different sky conditions and a navigation method based on the symmetry of the AOP map of skylight[J]. *Optics Express*, 2018, 26(22): 28589-28603.

[33] FAN C, HU X P, HE X F, *et al.* Integrated polarized skylight sensor and MIMU with a metric map for urban ground navigation[J]. *IEEE Sensors Journal*, 2018, 18(4): 1714-1722.

[34] FAN C, HU X P, HE X F, *et al.* Multicamera polarized vision for the orientation with the skylight polarization patterns [J]. *Optical Engineering*, 2018, 57(4): 043101.

[35] WANG Y L, CHU J K, ZHANG R, *et al.* Orthogonal vector algorithm to obtain the solar vector using the single-scattering Rayleigh model[J]. *Applied Optics*, 2018, 57(4): 594-601.

[36] WANG Y L, CHU J K, ZHANG R, *et al.* A bio-inspired polarization sensor with high outdoor accuracy and central-symmetry calibration method with integrating sphere [J]. *Sensors*, 2019, 19(16): 3448.

[37] LIANG H J, BAI H Y, LIU N, *et al.* Limitation of Rayleigh sky model for bioinspired polarized skylight navigation in three-dimensional attitude determination[J]. *Bioinspiration & Biomimetics*, 2020, 15(4): 046007.

[38] PALMER L, PALANKAR M. Blind hexapod walking over uneven terrain using only local feedback[C]. 2011 *IEEE International Conference on*

Robotics and Biomimetics. December 7-11, 2011, *Karon Beach, Thailand. IEEE*, 2011: 1603-1608.

[39] SAITO R, WATANABE K, NAGAI I. Laser odometry taking account of the tilt on the laser sensor[C]. 2015 10*th Asian Control Conference* (*ASCC*). *May* 31-*June* 3, 2015, *Kota Kinabalu*, *Malaysia. IEEE*, 2015: 1-4.

[40] GRENA R. An algorithm for the computation of the solar position[J]. *Solar Energy*, 2008, 82(5): 462-470.

[41] GRENA R. Five new algorithms for the computation of Sun position from 2010 to 2110[J]. *Solar Energy*, 2012, 86(5): 1323-1337.

[42] BOURGES B. Improvement in solar declination computation[J]. *Solar Energy*, 1985, 35(4): 367-369.

[43] REDA I, ANDREAS A. Solar position algorithm for solar radiation applications[J]. *Solar Energy*, 2004, 76(5): 577-589.

[44] BRINES M L, GOULD J L. Skylight polarization patterns and animal orientation[J]. *Journal of Experimental Biology*, 1982, 96(1): 69-91.

作者简介:

梁华驹(1993－),男,安徽合肥人,博士研究生,2016年于南京理工大学获得学士学位,主要从事弹箭组合导航与偏振光导航的研究。E-mail: lianghuaju@sina.cn

通讯作者:

白宏阳(1985－),男,陕西宝鸡人,博士,副教授,2007年、2012年于南京理工大学分别获得学士、博士学位,主要从事弹箭组合导航与末制导技术,目标识别的研究。E-mail: hongyang@njust.edu.cn